Journal of Medical Robotics Research, Vol. 0, No. 0 (2015) 1–7

MAPS – a Magic Angle Positioning System for Enhanced Imaging in High-Field Small-Bore MRI

Alexander Squires[1], Kevin C. Chan[2-5], Leon C. Ho[2,6], Ian A. Sigal[2-4], Ning-Jiun Jan[2-3] and Zion Tsz Ho Tse[1*]

[1]*Medical Robotics Lab, College of Engineering, The University of Georgia, Athens, GA, USA;*

[2]*UPMC Eye Center, Ophthalmology and Visual Science Research Center, Department of Ophthalmology, School of Medicine;*

[3]*Department of Bioengineering, Swanson School of Engineering;*

[4]*McGowan Institute for Regenerative Medicine, University of Pittsburgh, Pittsburgh, PA, USA;*

[5]*Center for the Neural Basis of Cognition, University of Pittsburgh and Carnegie Mellon University, Pittsburgh, PA, USA;*

[6]*Department of Electrical and Electronic Engineering, The University of Hong Kong, Pokfulam, Hong Kong, China*

The "magic angle" MRI effect can enhance signal intensity in aligned collagenous structures oriented at approximately 55° with respect to the main magnetic field. The difficulty of positioning tissue inside closed-bore scanners has hampered magic angle use in research and clinics. An MRI-conditional mechatronic system has been developed to control sample orientation inside a 9.4T small bore MRI scanner. The system orients samples to within 0.5˚ and enables a 600% increase in tendon signal intensity.

Keywords: Magic Angle Effect, Magnetic Resonance Imaging, MR-conditional, MR-safe

1. Introduction

The signal intensity obtained during MRI scans depends on a combination of natural factors (e.g. T1/T2 times, proton density, field inhomogeneity) and scan parameters (e.g. repetition time/echo time (TR/TE), flip angle) (1). In highly ordered tissues, water molecules are somewhat restricted in their movement, causing increased spin-spin interactions. These interactions reduce transverse relaxation times (T2), reducing signal intensity at a rate proportional to $3 \cdot \cos(2\theta)-1$, where θ is the angle between the primary magnetic field (B_o) and the direction in which the spins are coupled (1,2). By choosing a signal reduction of 0% (i.e. the maximum signal intensity) the equation returns $\theta=54.74°$, frequently simplified to 55°. This angle is referred to as the "magic angle" and the increase in Signal-to-Noise Ratio (SNR) is known as the magic angle effect (2,3).

Utilizing this effect, it is possible to obtain high-quality images of fibrous microstructures (3,4). With a small-bore scanner, high-resolution images comparable to histology are obtainable without damaging tissue, allowing analysis of living tissues and comparison between in vivo and ex vivo samples (5,6). Use of a small-bore, high-field scanner provides an improved signal-to-noise ratio over clinical scanners, delivering a boost in image quality useful when performing functional MRI, microscopic MRI, or other procedures requiring a high resolution in a small field of view (5,7,8).

While MRI provides excellent image quality, complications present themselves when developing peripheral devices for use in MR environments for basic and translational MRI research (9-11). Safety concerns for MR-conditional devices prohibit certain materials from being used in their design (12). The intense magnetic field eliminates ferro-/para-magnetic materials from design consideration. After safety considerations are met, image quality concerns must be considered; any component which functions based on electromagnetic principles can cause image artifacts (9,13,14). In particular, small-bore scanners present difficulties in mechanical design for any application requiring actuation inside environments where space is at a premium.

Taking advantage of the magic angle effect requires precise positioning and orientation of the sample, as demonstrated in the results; a 5˚ difference in orientation decreased intensity by almost two-thirds (2-4). The goal of the presented MAPS is to streamline the iterative process required for imaging fiber tissue structure using the magic angle effect, where precise adjustments are needed repeatedly for magic angle effect to be taken place at different segments of the tissue of the interest. Precise rotation of the sample by a motorized stage could allow the sample to be within the image field of view for comparison without repositioning of the tissue sample and the imaging coil. Thus, we have developed an MR-conditional mechatronic system for positioning and orienting samples inside a 9.4T small bore MRI scanner. Our goal with this manuscript is to describe this device, discuss the design requirements, present validation data and demonstrate its use.

2. Materials and Methods

2.1. *Design specifications*

Any device designed to operate in the MRI environment must be safe in the high-strength magnetic field, which can be

accomplished by using non-magnetic materials in the device's design. While non-magnetic metals may be safely used inside the scanner, those materials with high magnetic susceptibility can produce magnetic field inhomogeneity and image artifacts that may negatively affect image quality and provide image voids (13,15). To satisfy both safety and image quality considerations, our MRI sample positioning platform was designed and fabricated entirely from acrylonitrile butadiene styrene (ABS, a type of thermoplastic) components. Spatial restrictions were also important. The positioner would be used in a small-bore horizontal MRI scanner with inserts which limited the effective bore diameter up to 11cm. Tissue samples were placed on a 6cm diameter turntable and contained inside test tubes. To meet the positioning needs of the current projects, the accuracy goal for the device's turntable orientation was positioning error at or below 0.5°.

(a) MAPS setup schematic in MRI suite

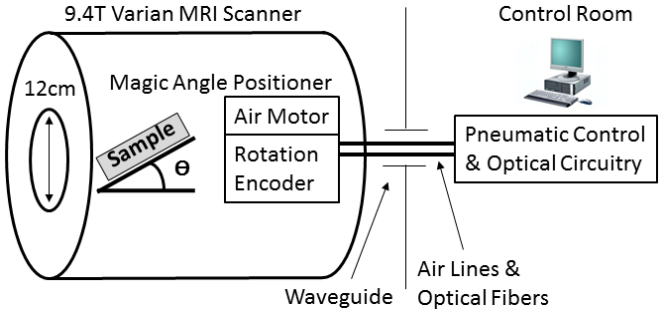

(b) Block diagram of MAPS and control box

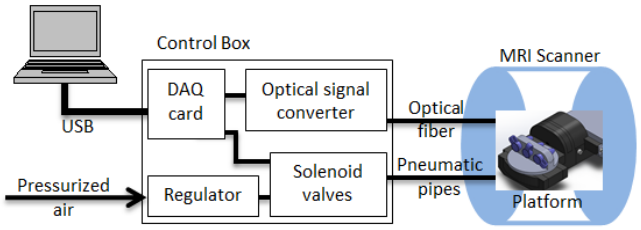

(c) Magic Angle Positioner (d) Exploded view

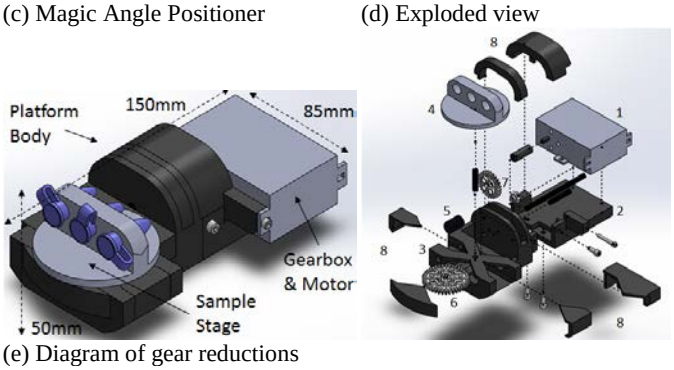

(e) Diagram of gear reductions

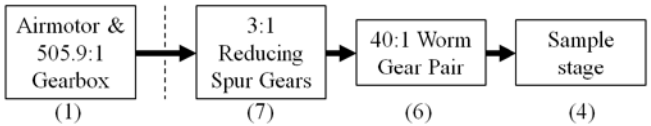

Figure 1 – Overview of the Magic Angle Positioning System: (a) Positioner setup in 9.4T small bore, horizontal scanner. (b) Diagram of control circuitry. (c) The assembled sample positioning platform. (d) Exploded view of the sample positioning platform. (e) Block diagram of gear reductions, with numbers below the blocks correlating to Fig. 1d and Table 1.

The specification of positioning resolution was established by consulting the collaborating radiologist and MRI physicist on the project team. The magic angle effect has been adopted clinically to enhance the contrast and SNR of tendinous tissue in MR images (16-18), and from the literature, the clinical protocols for positioning the tissue of interest use a positioning accuracy of 1˚-5˚. Therefore, a goal of 0.5˚ positioning resolution is enables the practical use of the device for fast and repeatable positioning in magic angle related studies. Use of a motorized sample positioning platform allows adjustment of sample position to be performed while maintaining the position of the sample stage and MR coils and eliminating the need for repeated movement of the gantry in and out of the bore, streamlining procedures in which multiple adjustments need to be made. Additionally, misalignments when initially loading samples can be compensated for once initial scans have been taken.

2.2. *Overview of the Magic Angle Positioning System*

The Magic Angle Positioning System (MAPS) is composed of three primary components: the computer interface, the control box, and the sample positioning platform (Figure 1). The computer interface provides selection of control modes and angular information. The control box, placed 2 meters from the scanner gantry, houses the valves, fiber optic circuitry, and other electronics necessary to operate the MAPS. The sample positioning platform utilizes pneumatic power to rotate samples inside the bore of the scanner. Additionally, a connecting cable between the control box and the sample positioning platform was assembled.

The computer interface, programmed in LabView®, provides a Graphical User Interface (GUI) for operating the MAPS. Operators may choose between either manual or automatic positioning modes, depending on preferences and application. Manual control provides the operator with the

Table 1 – Sample Positioning Platform Components (from Fig.1d-e)

#	Component	Dimensions, etc.
1	Motor & Tamiya Gearbox	68x45x27 mm
2	Gearbox Support Body	72x80x30 mm
3	Sample Stage Support Body	85x80x45 mm
4	Sample Stage	Ø55x24 mm
5	Sample Stage Gear	Ø42 mm (40 teeth)
6	Worm Gear	16 mm (3 teeth engaged)
7	Spur Gear Pair	3:1 (24:8 teeth)
8	Assorted Covers	6 different covers

choice to rotate the sample platform either clockwise or counter-clockwise. Automatic positioning allows the computer to position the sample platform using a proportional control (19).

The control box is an aluminum enclosure to ensure it is MRI-conditional. The computer interface connects to a National Instruments USB-6009 digital acquisition card, which controls a motor driver and collects signals from a fiber optic kit. The dual H-bridge motor driver (Sparkfun, ROB-09670) provides the power necessary to operate a pair of solenoid valves (ALCON, 01AA031B1-4PCA) which control the airflow that powers the pneumatic motor. The fiber optic kit (Carl's Electronics, CK1500) relayed the rotation of the sample platform. The connection between the control box and the positioning platform consisted of four 1mm fiber optic cables and a pair of 2.8mm ID plastic pneumatic pipes, both of which were outfitted with quick-connect fittings to facilitate ease in transportation and assembly.

The positioning platform (Figure 1c) was comprised of 3-Dimensional (3D) printed ABS plastic parts and commercial plastic components, and consisted of two separate sections. The first was a motor housing to hold the pneumatic motor (Figure 1d), the fiber optic supports, and the initial 505.9:1 Tamiya gearbox (TAMIYA Inc., 72005). The second section shifted the axle down and laterally through a 3:1 spur gear combination, then into a 40:1 worm gear (Fig. 1d-e). A pair of sample holders was also 3D printed: the first was a flat platform with a ring of holes to act as attachment points for adaptability, while the second could secure samples contained in micro-centrifuge tubes. Due to being constructed entirely from plastic components, pneumatic actuation, and encoding rotation via optical fibers, a complete lack of electrical components in the platform was achieved, eliminating image fidelity concerns and safety issues due to electrical interference.

2.3. *Platform Testing with MRI-Conditional Miniature Airmotor with Integrated Encoder*

The MRI environment imposes huge challenges for electromagnetic (EM) actuators. The static magnetic field, as well as the Radio-Frequency (RF) pulses and switched-magnetic-field gradients applied during imaging, interfere with the normal operation of electronics. Additionally, an EM actuator used in the MRI scanner room can degrade image quality due to EM noise emission (20-22). For these reasons, we developed the capability to accurately control a nonmetallic pneumatic actuator (Fig.2a) which can match the form factor of hobby DC motors (2.4 cm in diameter and 2.7 cm in height, Fig. 2b). A pair of fiber optic lines passed through the body of the motor to encode rotation. A pair of beam-interrupting arcs extended off the main shaft of the turbine rotor, providing a single period of quadrature encoding per revolution with an angular resolution of +/-90° (Fig.2e). Compressed air drove the turbine, after which a 60,708:1 gear reduction was accomplished via a 505.9:1 reducing gearbox, a 3:1 spur gear pairing, and a 40:1 worm gear. Plastic ball bearings with polyacetal races, glass balls, and nylon cages were added to the air turbine shaft to reduce friction. Control of the airmotor was accomplished with solenoid air valves, which limited the dynamic response of the control system; this drawback was overcome by controlling the motor with proportionally smaller pulses of air as the motor neared its goal position, timed such that the motor completely stopped before the application of the next pulse. A deadband halted the application of pressure once

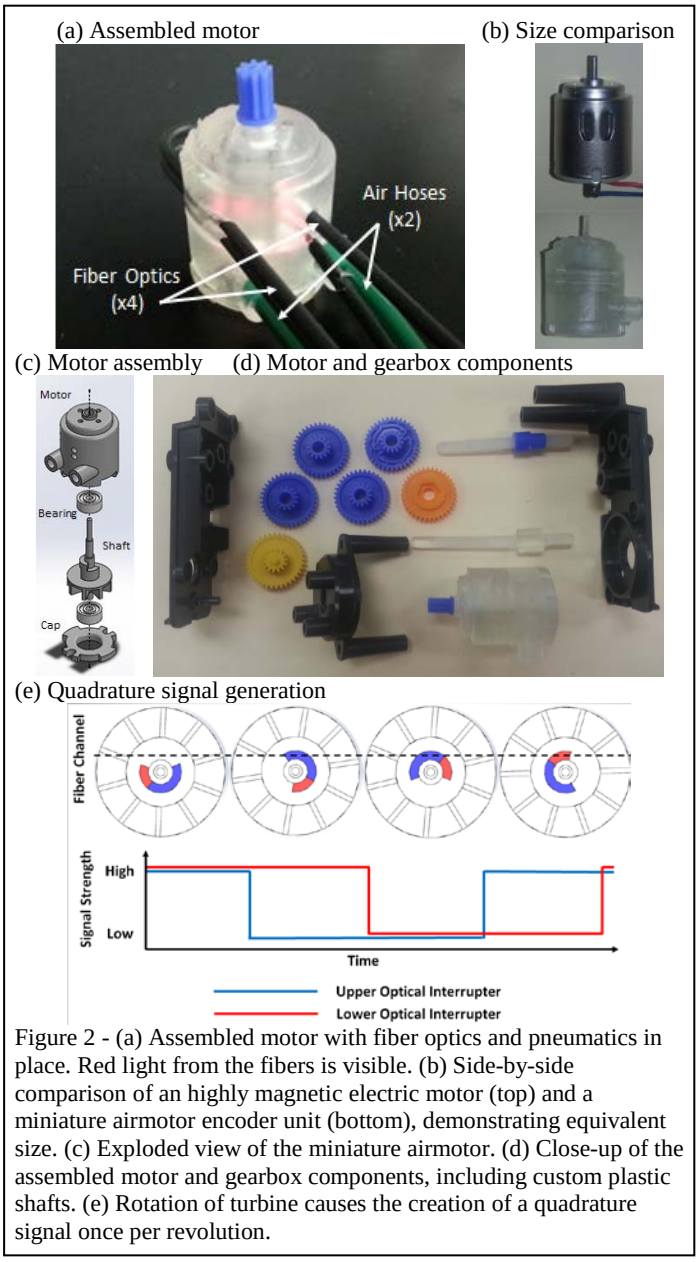

Figure 2 - (a) Assembled motor with fiber optics and pneumatics in place. Red light from the fibers is visible. (b) Side-by-side comparison of an highly magnetic electric motor (top) and a miniature airmotor encoder unit (bottom), demonstrating equivalent size. (c) Exploded view of the miniature airmotor. (d) Close-up of the assembled motor and gearbox components, including custom plastic shafts. (e) Rotation of turbine causes the creation of a quadrature signal once per revolution.

within an acceptable error range. The development of this motor is an improvement over previous MR-compatible pneumatic motors, which lacked an integrated quadrature system, instead relying on MR registration or external encoders for position information (18).

The completed system was first tested outside the scanner to ensure accuracy and determine the motor's load capabilities for further testing. Platform accuracy was quantified with a quadrature encoder generating 1024 pulses/revolution, giving a resolution of 0.088° (YUMO Corporation, E6B2-CWZ3E). Unloaded trials at different pressures were used to quantify system accuracy by rotating the output shaft by a specific amount. Loaded trials demonstrated the platform's performance, measured by loading the output shaft of the of the platform in 50g increments from 0g to 500g until the current pressure was incapable of generating the force required to actuate the platform. Trials varied the pressure from 20 to 40 PSI.

2.4. *Image Acquisition*

The MAPS facilitated a series of imaging tests of fibrous tissues using loaded and unloaded ovine Achilles' tendons embedded in agarose gel. System calibration was conducted during the tissue localization scan. Once the initial scan was conducted, the offset angle between B_0 and the principal axis of the tissue sample is used to initialize tissue position and updated when the platform is rotated. Measuring the impact the positioning platform exerted on MR images was performed in a 9.4T Varian/Agilent horizontal MRI scanner, used due to its ability to produce high-resolution images when studying the magic angle effect in a small tissue sample. Two-dimensional high-resolution multi-slice spin echo pulse sequences were used with repetition time = 1000ms, echo time = 13.2ms, and in-plane resolution 60x60 μm^2.

Specifications for defining and measuring artifacts were taken from ASTM standard F2119 (23), based on the parallels between unpowered MR-conditional implants and the unpowered sample platform. Image quality and SNR were evaluated in three conditions: MAPS absent, powered up and down (Fig. 4). A cylindrical phosphate buffered saline phantom was imaged with a standard multi-slice spin echo sequence. The SNR of the image with only the phantom was computed using the formula

$$SNR = \mu/\sigma \quad (1)$$

where μ is the mean signal in the 9mm x 9mm region of interest (ROI) in the image center of the phantom (ROI-1) and σ is the standard deviation of the signal in the 9mmX9mm ROI at the right top corner of the image (ROI-2).

Tendons were initially scanned with their primary orientation parallel to the main magnetic field B_o. Defining this as relative 0° to B_0, the samples' rotations were incremented up to the magic angle (~55° relative to B_0), and continued to 90° relative to B_0. Using the standard deviation of surrounding agarose gel as the reference measurement for noise, the signal intensity resulting from the magic angle is measured as the SNR of target structures relative to the surrounding gel.

3. Results and Discussion

3.1. *Platform Accuracy*

The magic angle platform was operated in the pressure range of 20 to 40 PSI. Figure 3(a) shows the positioning error in for different target angles and pressure levels. The magic angle platform demonstrated a maximum error of 0.27° as shown in Figure 2(a), a mean error of 0.020˚, and a standard deviation of 0.073˚ for rotation from all the error measurements (n=180).

Figure 3(b) shows the magic platform under varying load conditions. Load conditions were tested by operating the platform from the initial position of 0˚ (parallel to the B_0) to the magic angle of 55˚, during which average speed, measured position, and actual position were recorded. While maximum positioning error over all conditions (pressure, target, and load) was 0.27°, all but one condition resulted in error within 0.18˚ of the target. The termination of each pressure condition represented the final load which the system was able to actuate before being unable to generate the requisite torque. Fig. 2(b) demonstrates a linear performance of the motor speed versus the delivery torque under air pressure from 20 PSI to 40PSI, where the motor speed increased with the air pressure level.

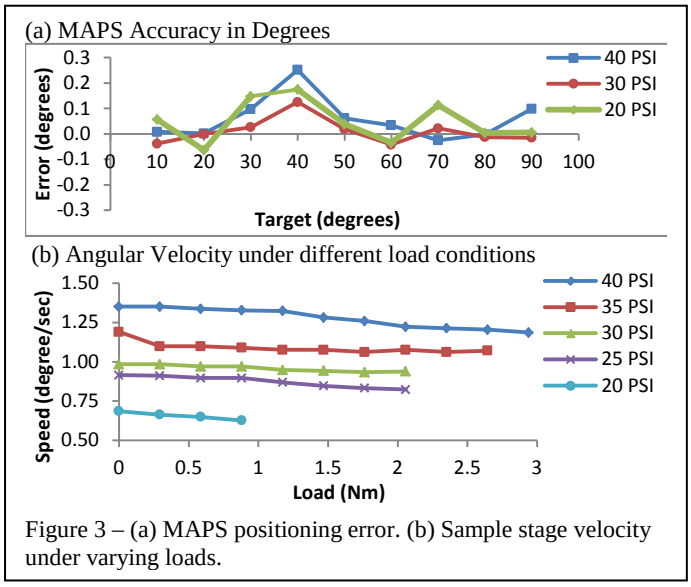

Figure 3 – (a) MAPS positioning error. (b) Sample stage velocity under varying loads.

3.2. *MRI Compatibility*

The results of SNR validation experiments are displayed in Fig. 4; less than 1% SNR difference between the three conditions, demonstrating minimal effect from the system to the MRI images (24,25); no observable image artifacts existed when MAPS was present.

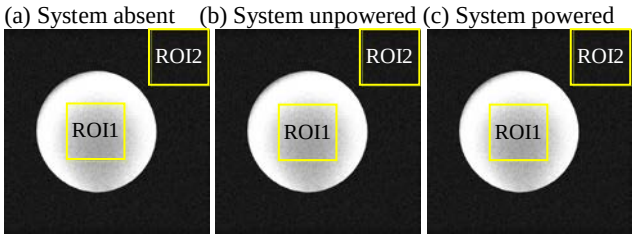

Figure 4 - Saline phantom when the sample positioning platform is (a) absent, (b) unpowered and (c) powered up. The yellow square indicates the 9mm x 9mm regions of interest (ROI) for SNR measurement. SNR variation is less than 1% between (a), (b), and (c).

(a) Comparison of results between unloaded and loaded tendons in various orientations

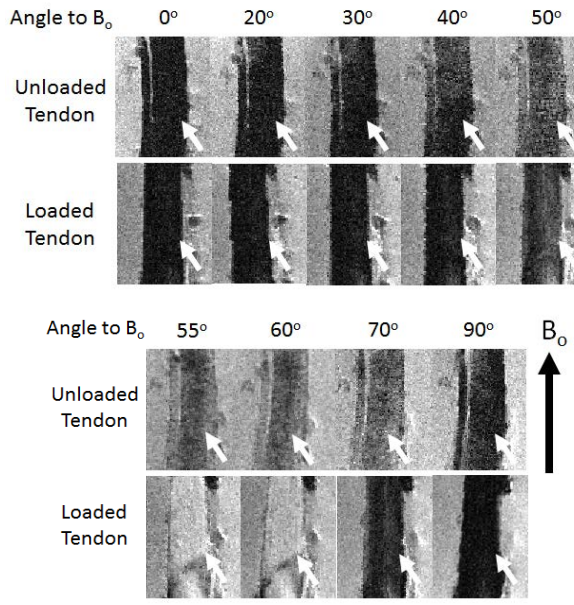

(b) SNR results from above images

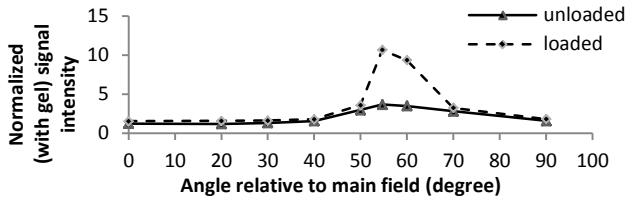

Figure 5 - (a) Magic angle effect in unloaded (top) and loaded (bottom) tendons (white arrows) at 9.4T MRI at 60x60 µm2. Note the signal enhancement near the magic angle (~55˚ to B_0). (b) Normalized signal intensity of unloaded (solid line) and loaded (broken line) tendons from 0°to 90° to main magnetic field (B_0).

(a) Histology, unloaded tendon (b) Histology, loaded tendon

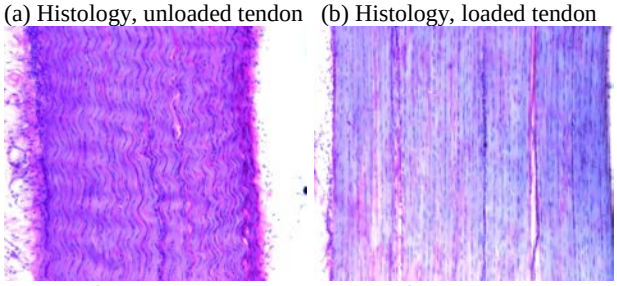

Crimping Striation

Figure 6 - Histological images of the tendons illustrating the orientation of the collagen fibers in unloaded (a) and loaded (b). The magic angle effect is more significant in the loaded tendon due to a high degree of alignment, whereas in the unloaded tissue the signal is partially canceled out due to the unaligned nature of crimped fibers. (a) corresponds with the Unloaded Tendon rows in Fig. 4a, while (b) is a tendon under load, as the bottom row in Fig. 4a.

3.3. *High-field Magic Angle Enhanced MRI of Tendon*

The results in Figure 5 show an increase in relative signal intensity as both loaded and unloaded tendons draw near to the magic angle. As shown in Figure 5, an unloaded tendon had an increase in signal intensity at the magic angle of about 200% relative to that at 0° to B_0, whereas a loaded tendon had a greater signal intensity increase, up to approximately 600% relative to that at 0° to B_0. Normalized data is shown quantitatively in Figure 4b. SNR for signal intensity measurements was calculated with the same method as the MRI compatibility tests.

The undulating pattern of the collagen fibers in the unloaded tendon samples, known as “crimping” (26,27), shows up strongly near the magic angle as light and dark bands perpendicular to the main orientation of the tendon. Similarly, the striated patterns of the loaded tendon were most pronounced near the magic angle (Figure 5a, 55˚), consistent with the stretch of the collagen fibers and disappearance of the crimp observed in MR images and in histology (Figure 5a, 6a) (6).

The MR signals were higher in loaded than unloaded tendons near the magic angle by a factor of 2 to 3 (Figure 5b). This is, in part, because in loaded tendons, the collagen fibers are more aligned with one another, longitudinally to the tendon (28). This explains the increased signal at the magic angle, but not the slight increase in signal in loaded tendons at other angles. This could be because in highly ordered, collagen rich fibrous tissues, bound protons are subject to spin-spin interactions within a static magnetic field. An increase in the distance between protons in tendons, caused by stretching during loading, may reduce the spin-spin interactions and increase signal strength (6). Another possible explanation lies

in the release of water, which was bound within the tendon prior to loading, altering the T2 relaxation time constant (29).

4. Conclusion

A high-field, small-bore MRI-conditional positioning system was developed using a miniature pneumatic motor, intended to facilitate Magic Angle-related experiments evaluating microstructures in fibrous tissues for basic and translational MRI research. The hardware and software were designed to provide a simple and accurate solution (max error <0. 5˚) for studying magic angle effect in fibrous tissues within a high-field and small bore MRI scanner. The hardware for the intra-scanner component contained a unique motion-encoder unit in conjunction with a reduction gearbox to accomplish highly accurate positioning of a sample platform for studies. The positioning platform demonstrated high levels of accuracy, positioning diminutive fibrous tissue samples in a small-bore scanner without the need for manual adjustment. Furthermore, the total lack of metallic components or electrical signals permitted high-resolution imaging free of image artifacts and radiofrequency electromagnetic interference. The use of custom 3D printed pneumatic actuators and encoder components drove the cost of the system down.

Validation of the system as a research tool was performed in unloaded and loaded tendon samples in which images demonstrated 200%-600% increase in SNR using the system. With the positive results generated, this system has demonstrated its practical usability in magic angle studies and other experiments that requires precise positioning within high-field small bore MRI scanners.

5. Funding Sources

Funding Support: This work was supported by the National Institutes of Health Contracts P30-EY008098, R01-EY-023966 and UL1-TR000005 (Bethesda, Maryland); BrightFocus Foundation G2013077 (Clarksburg, Maryland); Eye and Ear Foundation (Pittsburgh, Pennsylvania); and Research to Prevent Blindness (New York, New York).

6. Disclosures

The authors have no disclosures to declare.

References

1. Erickson SJ, Prost RW, Timins ME. The Magic-Angle Effect - Background Physics and Clinical Relevance. Radiology 1993;188(1):23-25.
2. Xia Y. Magic-angle effect in magnetic resonance imaging of articular cartilage - A review. Invest Radiol 2000;35(10):602-621.
3. Fullerton GD, Cameron IL, Ord VA. Orientation of Tendons in the Magnetic-Field and Its Effect on T2 Relaxation-Times. Radiology 1985;155(2):433-435.
4. Ho LC, Sigal IA, Jan N-J, Squires A, Tse Z, Wu EX, Kim S-G, Schuman JS, Chan KC. Magic angle-enhanced MRI of fibrous microstructures in sclera and cornea with and without intraocular pressure loading. Investigative ophthalmology & visual science 2014;55(9):5662-5672.
5. Chang EY, Du J, Bae WC, Statum S, Chung CB. Effects of achilles tendon immersion in saline and perfluorochemicals on T2 and T2*. Journal Of Magnetic Resonance Imaging: JMRI 2014;40(2):496-500.
6. Mountain KM, Bjarnason TA, Dunn JF, Matyas JR. The functional microstructure of tendon collagen revealed by high-field MRI. Magnetic Resonance In Medicine: Official Journal Of The Society Of Magnetic Resonance In Medicine / Society Of Magnetic Resonance In Medicine 2011;66(2):520-527.
7. Wang N, Kahn D, Badar F, Xia Y. Molecular origin of a loading-induced black layer in the deep region of articular cartilage at the magic angle. Journal Of Magnetic Resonance Imaging: JMRI 2014.
8. Schick F. Whole-body MRI at high field: technical limits and clinical potential. European Radiology 2005;15(5):946-959.
9. Elhawary H, Zivanovic A, Davies B, Lamperth M. A review of magnetic resonance imaging compatible manipulators in surgery. P I Mech Eng H 2006;220(H3):413-424.
10. Gassert R, Yamamoto A, Chapuis D, Dovat L, Bleuler H, Burdet E. Actuation methods for applications in MR environments. Concept Magn Reson B 2006;29B(4):191-209.
11. Tsekos NV, Khanicheh A, Christoforou E, Mavroidis C. Magnetic resonance - Compatible robotic and mechatronics systems for image-guided interventions and rehabilitation: A review study. Annu Rev Biomed Eng 2007;9:351-387.
12. ASTM. "Standard Practice for Marking Medical Devices and Other Items for Safety in the Magnetic Resonance Environment". Volume F2503.
13. Schenck JF. The role of magnetic susceptibility in magnetic resonance imaging: MRI magnetic compatibility of the first and second kinds. Med Phys 1996;23(6):815-850.
14. Shellock FG. Magnetic resonance safety update 2002: Implants and devices. J Magn Reson Imaging 2002;16(5):485-496.

15. Rudisch A, Kremser C, Peer S, Kathrein A, Judmaier W, Daniaux H. Metallic artifacts in magnetic resonance imaging of patients with spinal fusion. A comparison of implant materials and imaging sequences. Spine 1998;23(6):692-699.
16. Elhawary H, Zivanovic A, Rea M, Tse Z, McRobbie D, Young I, Paley M, Davies B, Lampérth M. A MR Compatible Mechatronic System to Facilitate Magic Angle Experiments in Vivo. In: Ayache N, Ourselin S, Maeder A, editors. Medical Image Computing and Computer-Assisted Intervention – MICCAI 2007. Volume 4792, Lecture Notes in Computer Science: Springer Berlin Heidelberg; 2007. p 604-611.
17. Elhawary H, Zivanovic A, Tse ZTH, Rea M, Davies BL, Young I, Bydder G, Payley M, Lamperth MU. A magnetic-resonance-compatible limb-positioning device to facilitate magic angle experiments in vivo. Proceedings of the Institution of Mechanical Engineers, Part H: Journal of Engineering in Medicine 2008;222(5):751-760.
18. Zion Tsz Ho T, Elhawary H, Zivanovic A, Rea M, Paley M, Bydder G, Davies BL, Young I, Lamperth MU. A 3-DOF MR-Compatible Device for Magic Angle Related <emphasis emphasistype="italic">In Vivo</emphasis> Experiments. Mechatronics, IEEE/ASME Transactions on 2008;13(3):316-324.
19. Åström KJ, Hägglund T. PID controllers: theory, design, and tuning. Instrument Society of America, Research Triangle Park, NC 1995.
20. ASTM-F2182. Standard Test Method for Measurement of Radio Frequency Induced Heating On or Near Passive Implants During Magnetic Resonance Imaging2011.
21. Shellock FG. Metallic surgical instruments for interventional MRI procedures: evaluation of MR safety. J Magn Reson Imaging 2001;13(1):152-157.
22. Elhawary H, Tse ZTH, Hamed A, Rea M, Davies BL, Lamperth MU. The case for MR-compatible robotics: a review of the state of the art. The International Journal of Medical Robotics and Computer Assisted Surgery 2008;4(2):105-113.
23. ASTM. Standard Test Method for Evaluation of MR Image Artifacts from Passive Implants. Volume F2119. West Conshohocken, PA: ASTM International; September 2007.
24. Chinzei K, Kikinis R, Jolesz F. MR Compatibility of Mechatronic Devices: Design Criteria. In: Taylor C, Colchester A, editors. Medical Image Computing and Computer-Assisted Intervention – MICCAI'99. Volume 1679, Lecture Notes in Computer Science: Springer Berlin Heidelberg; 1999. p 1020-1030.
25. Chinzei K, Hata N, Jolesz F, Kikinis R. MR Compatible Surgical Assist Robot: System Integration and Preliminary Feasibility Study. In: Delp S, DiGoia A, Jaramaz B, editors. Medical Image Computing and Computer-Assisted Intervention – MICCAI 2000. Volume 1935, Lecture Notes in Computer Science: Springer Berlin Heidelberg; 2000. p 921-930.
26. Rigby BJ, Hirai N, Spikes JD, Eyring H. The Mechanical Properties of Rat Tail Tendon. The Journal of General Physiology 1959;43(2):265.
27. Viidik A, Ekholm R. Light and electron microscopic studies of collagen fibers under strain. Zeitschrift für Anatomie und Entwicklungsgeschichte 1968;127(2):154.
28. Lake SP, Miller KS, Elliott DM, Soslowsky LJ. Effect of fiber distribution and realignment on the nonlinear and inhomogeneous mechanical properties of human supraspinatus tendon under longitudinal tensile loading. Journal of Orthopaedic Research 2009;27(12):1596-1602.
29. Hannafin JA, Arnoczky SP. Effect of cyclic and static tensile loading on water content and solute diffusion in canine flexor tendons: an in vitro study. Journal Of Orthopaedic Research: Official Publication Of The Orthopaedic Research Society 1994;12(3):350-356.